Journal of Solid State Chemistry 184 (2011) 2329–2332

Contents lists available at ScienceDirect

Journal of Solid State Chemistry

journal homepage: www.elsevier.com/locate/jssc

Structural changes of $(K,Gd)_2Ta_2O_7$ pyrochlore at high pressure

F.X. Zhang [a,*], M. Lang [a], J.M. Zhang [a], R.C. Ewing [a,*], M. Nyman [b]

[a] Department of Geological Science, The University of Michigan, Ann Arbor, MI 48109, USA
[b] Sandia National Laboratories, P.O. Box 5800, Albuquerque, NM 87185, USA

ARTICLE INFO

Article history:
Received 4 May 2011
Received in revised form
27 June 2011
Accepted 28 June 2011
Available online 3 July 2011

Keywords:
Tantalate pyrochlore
High pressure
XRD
Raman

ABSTRACT

The structure of K-bearing tantalate pyrochlore $(K_{2-x}Gd_x)Ta_2O_{6+x}(x\sim0.4)$ was studied at high pressures using *in situ* X-ray diffraction and Raman scattering methods. Experimental results indicated that $(K_{2-x}Gd_x)Ta_2O_{6+x}(x\sim0.4)$ retains the pyrochlore structure up to 40 GPa, but partial amorphization occurred at pressures above 23 GPa. The amorphous phase was also confirmed in the quenched sample by means of transmission electron microscopy. The tantalate pyrochlore lattice is more stable than pyrochlore compounds in other systems, such as rare earth titanates, zirconates and stannates. The structural stability of pyrochlore tantalate may be mainly related to the size ratio of cations on the 16*d* and 16*c* sites in the lattice.

Published by Elsevier Inc.

1. Introduction

Pyrochlore oxides $A_2B_2O_6O'$ crystallize in the cubic space group of $Fd\bar{3}m$. The structure can be regarded as a superlattice of fluorite AX_2, but cations A and B reside on two ordered 16*d* and 16*c* sites, respectively, and one-eighth oxygen atoms in the unit cell are missing. Pyrochlore oxides have a unique structure character in that both cations and anions can be deficient in the lattice simultaneously. The intrinsic disordering of cations and anions in the pyrochlore lattice leads to advanced physical and chemical properties that can be used in applications including ionic conductors, catalysts and electronic materials [1–5]. Due to the flexible structure, either the *A*-site or *B*-site can be partially replaced with actinide elements and form stable structures in a wide composition range and critical environmental conditions. Some pyrochlore oxides are thus regarded as promising candidate materials for nuclear waste storage in the future [6–8]. Based on the difference of cations in the unit cell, pyrochlore oxides can be divided into two major categories: $A_2^{3+}B_2^{4+}O_7$ and $A_2^{2+}B_2^{5+}O_7$. Transition metals Ti, Zr and group IVA element Sn usually form $A_2^{3+}B_2^{4+}O_7$ pyrochlores with rare earth elements. Transition metals of group IIB and VB form the second category pyrochlores. The stability of different pyrochlore compositions strongly depends on the size ratio of the cations R_A/R_B. At ambient conditions, rare earth pyrochlore is stable in the range of $R_A/R_B=$ 1.46–1.78 [9]. A distorted, defect-fluorite structure is stable if $R_A/R_B<1.46$. Some pyrochlore oxides with R_A/R_B ratio larger than the maximum value can only be synthesized at high-pressure conditions [10,11]. The doping of different cations on the *A* and *B* sites cannot only change the degree of disordering, but greatly influence the physical properties of pyrochlores [12,13]. Due to the large size difference of cations, alkaline-doped pyrochlores are seldom reported [14,15]. Recently, Nyman et al. [15] have successfully prepared alkaline-bearing pyrochlores in rare earth tantalates with a hydrothermal reaction method. The content of K in the pyrochlore structure depends on the synthetic conditions and the composition of the synthetic samples is determined by analyzing the final products.

In general, pyrochlore is a stable structure at ambient conditions; however, due to the intrinsic deficiency of cations and anions in the unit cell, the ordered pyrochlore structure can be disordered when exposed to various environments, such as energetic ion irradiation [16–20], high temperature [21] and high pressure [22–28]. In addition, a phase transition to a new dense polymorph was discovered at high pressure [23–27]. Details of the order–disorder transition in pyrochlores oxides induced by ion irradiation are summarized in Refs. [28,29], and the structural response at high pressure is given in Ref. [30]. In this paper, the structural behavior of K-bearing tantalate pyrochlore at high pressures was investigated by *in situ* X-ray diffraction (XRD) and Raman scattering measurements.

2. Experimental methods

The tantalate pyrochlore was synthesized by a hydrothermal method using $K_8[Ta_6O_{19}]\cdot xH_2O$ polyoxometalate salt, combined

* Corresponding authors.
E-mail addresses: zhangfx@umich.edu (F.X. Zhang), rodewing@umich.edu (R.C. Ewing).

0022-4596/$ - see front matter Published by Elsevier Inc.
doi:10.1016/j.jssc.2011.06.040

with alkaline-soluble lanthanum citrate complex. The details of the procedure are described elsewhere [15]. Transmission electron microscopy (TEM) observation verified the nano-size of synthesized powder, and X-ray diffraction (XRD) measurement confirmed the single phase pyrochlore structure.

For high-pressure experiments, a symmetric-type diamond anvil cell was used with a culet size of the anvils of 400 μm. The structure of the tantalate at ambient conditions was measured at Cornell High Energy Synchrotron Source (CHESS). The *in situ* XRD measurements at high pressure were performed at the X17C station of the National Synchrotron Light Source (NSLS), Brookhaven National Laboratory. The X-ray beam was monochromized to a wavelength of 0.4066 Å and the beamsize was less than 30 μm. A small amount of sample was loaded into a chamber of 120 μm diameter drilled in the center of a pre-indented stainless steel gasket with thickness of ~40 μm. The pressure medium was a mixture of methanol/ethanol (4/1 in volume), and the pressure was calibrated with the standard ruby fluorescence method [31]. All X-ray diffraction images were collected with a Mar 256 CCD detector, and the one-dimensional patterns were integrated from the images with the Fit2D software [32]. The lattice information was derived from the XRD profiles by Rietveld refinement using the program Fullprof [33].

The Raman measurements were conducted with a 514.5 nm green Ar ion laser, and spectra were collected with a liquid nitrogen cooled CCD detector. The sample quenched from high pressure was further analyzed with a JEOL 2010 transmission electron microscope and the cations in the sample were analyzed with X-ray energy dispersive spectroscopy.

3. Results and discussions

The XRD pattern of the as-prepared tantalate oxide is typical for pyrochlore and can be well refined with the $A_2B_2O_7$ structure model (Fig. 1). The lattice parameters and the K/Gd ratio were all refined with the measured XRD pattern. The refined lattice parameter of the cubic unit cell is 10.496(2) Å. The refinement indicated that for a best fitting, the K^+ and Gd^{3+} ions occupy the eight-coordinated 16*d* site, and Ta occupies the smaller six-coordinated octahedral site. The K/Gd ratio was also derived from the refinement. In order to keep charge balance, the oxygen at 48*f* site with a *x*-coordinate of 0.432(2) is not fully occupied. The specific composition of the powder used in this study can be written as $(K_{2-x}Gd_x)Ta_2O_{6+x}(x\sim0.4)$ based on the Rietveld refinement. The conventional Rietveld factor for the pattern at ambient conditions is $R_{wp}=17.6\%$ and the Bragg factor $R_B=6.4\%$.

The evolution of the XRD patterns with pressure is illustrated in Fig. 2. The peak width of the diffractions increases at high pressures, especially at pressures above 13 GPa. The non-ideal hydrostatic pressure conditions in the sample chamber may be an important contribution to the peak broadening, because the pressure transmitting medium used in this study (methanol ethanol mixture) provides only hydrostatic pressure below ~10 GPa. A diffuse scattering close to the strongest diffraction maximum [2 2 2] becomes visible at pressure above 30 GPa, which is a clear evidence of pressure-induced amorphization of $(K_{2-x}Gd_x)Ta_2O_{6+x}(x\sim0.4)$. This is similar to $Gd_2Ti_2O_7$ pyrochlore for which amorphization has been also observed during pressurization [25]. However, the tantalate pyrochlore cannot be completely amorphized even to the highest pressure used in this study (42 GPa). The [1 1 1] diffraction of pyrochlore structure at ~4° of two theta angle is clearly observable, which demonstrates that a small amount of pyrochlore structure persists up to this pressure. After pressure release, all the pyrochlore diffractions increase in intensity and become narrower. The later process indicates that the peak broadening at high pressure was mainly caused by the non-hydrostatic pressure conditions in the sample. The broad diffuse scattering of the amorphous phase can be seen in the pattern of the quenched sample; thus the partial amorphization process is irreversible. Except crystalline-to-amorphous transformation, no other pressure-induced phase transition was observed in $(K_{2-x}Gd_x)Ta_2O_{6+x}(x\sim0.4)$. This is a significantly different behavior compared to rare earth titanate and zirconate with pyrochlore structures [22–27]. All pyrochlore-structured zirconates transform under pressure to a distorted cotunite-type high-pressure phase starting at pressures around 20 GPa. For the rare earth titanates, a similar transition occurred but at higher pressures. However, this phase transition cannot be complete in

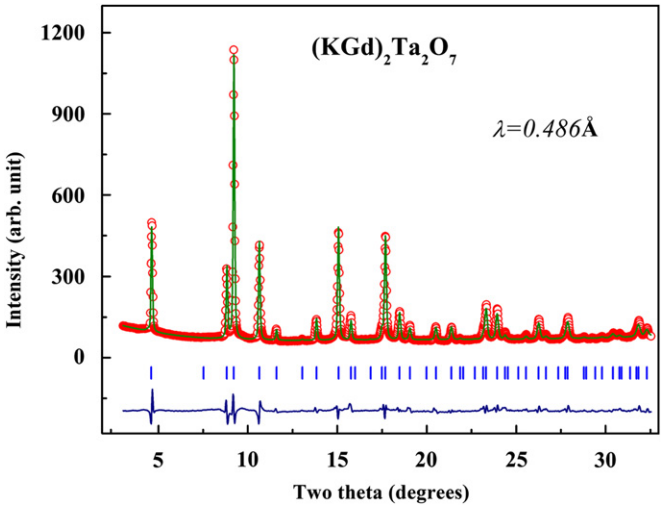

Fig. 1. Observed XRD pattern of $(K_{2-x}Gd_x)Ta_2O_{6+x}(x\sim0.4)$ at ambient conditions is well refined with a pyrochlore structure model. Symbols and line represent observed and calculated XRD patterns, respectively. The curve at the bottom is their difference and the vertical bars represent the position of Bragg peaks.

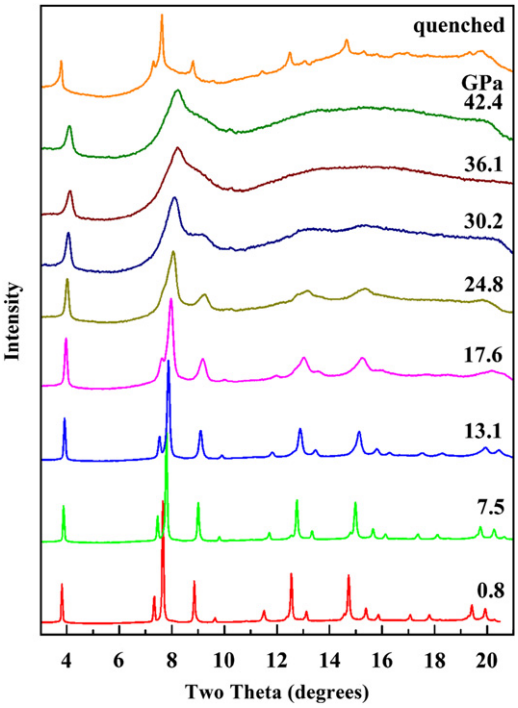

Fig. 2. Evolution of XRD patterns with external pressure (λ=0.4066 Å). After 30 GPa, an amorphous phase is observable and the amorphization process is irreversible.

those pyrochlores because a pressure-induced amorphization dominates at very high pressures. In fact, no cotunite-type high-pressure phase can form in $(K_{2-x}Gd_x)Ta_2O_{6+x}(x\sim0.4)$ might be related to the different size ratio of cations at the 16*c* and 16*d* site. Compared with rare earth titanates and rare earth zirconates, the tantalate pyrochlore used in this study has a much larger ratio R_A/R_B of cation sizes. In other words, the two cations of zirconate pyrochlores are rather comparable in size, which facilitate a cation disordering and related phase transformation under pressure. The energetic of the disordering process in different pyrochlore compositions has been compared by means of quantum mechanical calculations [25,34]. The pressure-induced phase transition is closely related to the degree of disorder in the pyrochlore structure because the cotunnite-type high-pressure phase is fully disordered at the cationic sublattice [22,35]. The larger cationic size ratio close to 1.78 for titanate pyrochlore is the reason for the higher transformation pressure compared with zirconates with ratio of ~1.46. With $R_A/R_B=1.98$ for the tantalate sample, the size difference is obviously too big to initiate formation of the high-pressure phase because the high pressure only has one cationic site. If the pressure is sufficiently high, the pyrochlore structure is directly transformed to the amorphous state.

As summarized in Ref. [37], pressure-induced amorphization is common to many materials and minerals. To tantalite pyrochlore, due to the large size difference between the cations on the *A*- and *B*-sites, it is interesting to compare the atomic disordering and structural stability with other pyrochlores during the pressurization process. The XRD patterns of $(K_{2-x}Gd_x)Ta_2O_{6+x}(x\sim0.4)$ at high pressures were analyzed with Rietveld refinement. At pressures larger than 30 GPa, significantly increased width of diffraction maxima and the appearance of the amorphous phase made a reliable procedure difficult, which is expressed in larger error bars for the derived lattice parameter. The compressibility of the unit cell is plotted in Fig. 3 as a function of pressure together with the 48*f* *x*-coordinate as inset. The x_{48f} parameter shows a slight decrease with the increase of pressure, which is indicative for a higher degree of anion disordering. However, the pressure dependence is much weaker than that in rare earth zirconate pyrochlores [26]. This demonstrates that pressure-induced anion disordering in the tantalate pyrochlore is also much smaller than rare earth zirconate pyrochlores. This explains again why this material persists to higher pressures without any phase transformation. Fitting the *P*–*V* curve with the Birch–Murnaghan equation of state yield a bulk modulus of $B_0=173(11)$ GPa when the pressure derivative at zero pressure is fixed at 4. The bulk modulus of $(K_{2-x}Gd_x)Ta_2O_{6+x}(x\sim0.4)$ is comparable with that of rare earth titanate pyrochlores, such as $Sm_2Ti_2O_7$ (165 GPa [35]) $Gd_2Ti_2O_7$ (176 GPa [36]), but a little smaller as for zirconates, such as $Gd_2Zr_2O_7$ (186 GPa [23]).

The Raman measurements at ambient conditions and at high pressure are shown in Fig. 4. Theoretically, a completely ordered pyrochlore lattice has five Raman active modes in the Brillouin center [24]. Due to the mixed occupancy of K^+ and Gd^{3+} in the 16*d* site and the intrinsic anion deficiency on the 48*f* site, the Raman spectrum of $(K_{2-x}Gd_x)Ta_2O_{6+x}(x\sim0.4)$ is rather complex compared to rare earth titante pyrochlores. The broad band after 600 cm^{-1} at ambient pressure is a contribution from a small amount of anion disordering in the starting sample. The mode at ~900 cm^{-1} at high pressures is due to the M/E pressure medium. With the increase of pressure, the Raman modes reduce their intensities. Starting at ~23.3 GPa, the amorphous phase can be clearly observed in the spectra (Fig. 4) as two broad bands at ~470 and 700 cm^{-1} [24]. The characteristics of the vibrational properties of amorphous $(K_{2-x}Gd_x)Ta_2O_{6+x}(x\sim0.4)$ is quite similar to the amorphous $Gd_2Ti_2O_7$ [24]. As function of increasing pressure up to 46.7 GPa, the intensity of the amorphous bands gradually increases, however, some crystalline remnants are present over the entire pressure range as evidenced by their vibrational modes in the low frequency region. After quenching the sample from 46.7 GPa, the Raman spectrum is similar with as the starting material before pressurization but with an additional broad band at ~780 cm^{-1} from the amorphous phase. Thus the recovered high-pressure sample is a mixture of amorphous and crystalline pyrochlore phase, which is consistent with the XRD measurements. Also no indication of a pressure-induced formation of a new crystalline phase was evident in the Raman measurements.

In addition to XRD and Raman measurements, the quenched sample was characterized by TEM analysis. Fig. 5 shows typical TEM bright field images of tantalate pyrochlore after the application of pressure. The large agglomerates are composed of many

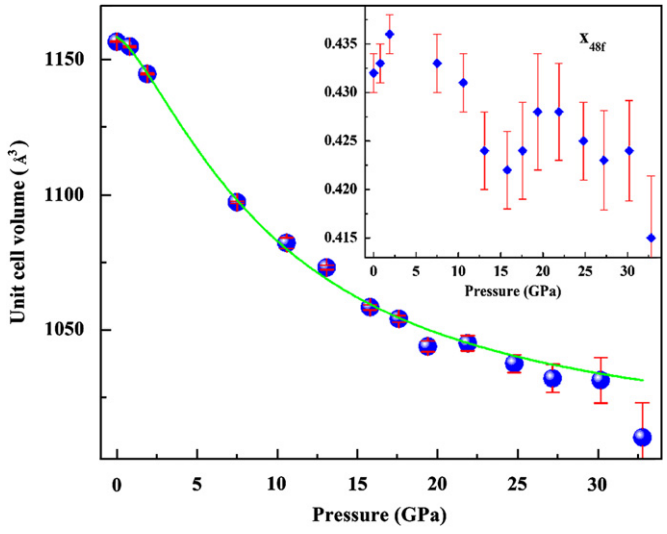

Fig. 3. *P*–*V* curve of $(K_{2-x}Gd_x)Ta_2O_{6+x}(x\sim0.4)$. Inset shows the pressure dependence of *x*-coordinate of oxygen at 48*f* site.

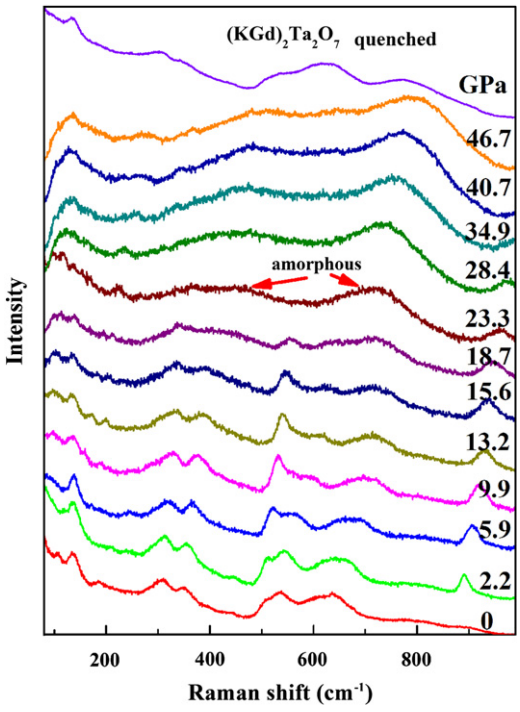

Fig. 4. Raman spectra of $(K_{2-x}Gd_x)Ta_2O_{6+x}(x\sim0.4)$ at various pressures. At pressures above 23.3 GPa, an amorphous phase is obviously identified.

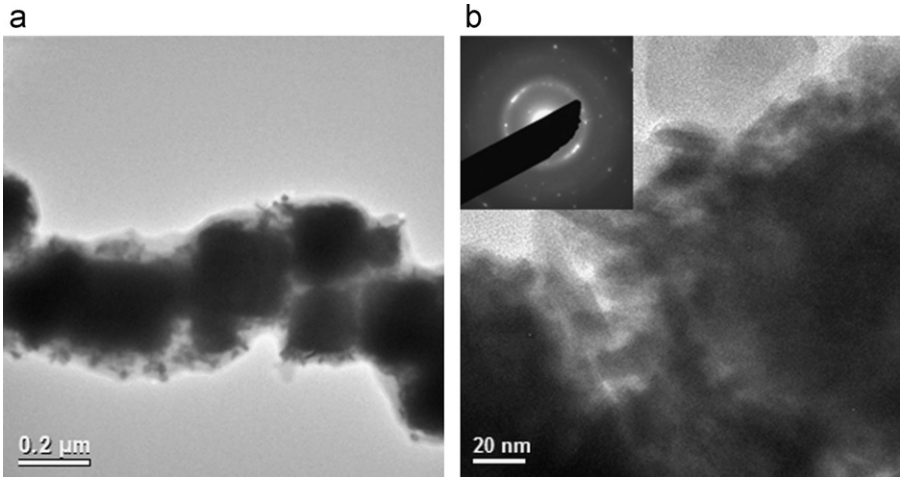

Fig. 5. TEM images of $(K_{2-x}Gd_x)Ta_2O_{6+x}(x\sim0.4)$ quenched from 46.7 GPa. The sample in (a) shows the agglomerates of nanoparticles. The inset in (b) shows the SEAD of the sample, which clearly indicates the mixture of crystalline and amorphous phases in the sample.

small grains with 10–20 nm in size (Fig. 5a). The selected area electron diffraction pattern (inset of Fig. 5b) shows the diffuse scattering from the amorphous phase next to the strongest diffraction spots from crystalline pyrochlore [2 2 2]. This independently confirms the mixed crystalline and amorphous quenched sample. The XEDS analysis of the sample suggested a molar ratio of 4/1 for the K^+ and Gd^{3+} ions, which is consistent with atomic ratio of 1.6/0.4 from the XRD refinement.

4. Summary

Hydrothermally synthesized nanocrystalline powders of $(K_{2-x}Gd_x)Ta_2O_{6+x}(x\sim0.4)$ with the pyrochlore structure was pressurized to 47 GPa. *In situ* synchrotron XRD and Raman measurements revealed that the ordered pyrochlore structure of tantalate oxide is very resistant to the application of pressure without the formation of a high-pressure phase. However, an irreversible partial amorphization was independently confirmed by XRD, Raman spectroscopy and TEM. The enhanced stability of the tantalate pyrochlore lattice can be explained by the large size difference of cations on the 16*d* and 16*c* sites.

Acknowledgment

This work was supported as part of the Materials Science of Actinides, an Energy Frontier Research Center, funded by the Office of Basic Energy Sciences under Award Number DE-SC0001089.The use of X-ray beam line at X17C station of NSLS is supported by NSF COMPRES EAR01-35554 and by US-DOE contract DE-AC02-10886.

References

[1] S.A. Kramer, H.L. Tuller, Solid State Ionics 82 (1995) 15.
[2] P.K. Moon, H.L. Tuller, Solid State Ionics 28–30 (1988) 470.
[3] M. Uno, et al., J. Alloys Compd. 420 (2006) 291.
[4] T. Omata, S. Otsuka-Yao-Matsuo, J. Electrochem. Soc. 148 (2001) E252.
[5] J.M. Sohn, M.R. Kim, S.I. Woo, Catal. Today 83 (2003) 289.
[6] W.J. Weber, R.C. Ewing, C.R.A. Catlow, T.D. de la Rubia, L.W. Hobbs, C. Kinoshita, H. Matzke, A.T. Motta, M. Nastasi, E.K.H. Salje, E.R. Vance, S.J. Zinkle, J. Mater. Res. 13 (1998) 1434.
[7] W.L. Gong, W. Lutze, R.C. Ewing, J. Nucl. Mater. 277 (2000) 239.
[8] S.X. Wang, B.D. Begg, L.M. Wang, R.C. Ewing, W.J. Weber, K.V.G. Kutty, J. Mater. Res. 14, 4470 (1999).
[9] M.A. Subramanian, G. Aravamudan, G.V. Subba Rao, J. Solid State Chem. 15 (1983) 55–143.
[10] M.A. Subramanian, Mater. Res. Bull. 27 (1992) 939.
[11] W. Cheihk-Rouhou, P. Strobel, C. Chaillout, S.M. Loureiro, R. Senis, B. Martinez, X. Obradors, J. Pierre, J. Mater. Chem. 9 (1999) 743.
[12] P.J. Wilde, C.R.A. Catlow, Solid State Ionics 112 (1998) 185.
[13] K.J. Moreno, A.F. Fuentes, M. Maczka, J. Hanuza, U. Amador, J. Santamaria, C. Leon, Phys. Rev. B 75 (2007) 184303.
[14] D.W. Murphy, J.L. Dye, S.M. Zahurak, Inorg. Chem. 22 (1983) 3679.
[15] M. Nyman, M.A. Rodriguez, L.E. Shea-Rohwer, J.E. Martin, P.P. Provencio, J. Am. Chem. Soc. 131 (2009) 11652.
[16] J. Lian, L.M. Wang, J. Chen, K. Sun, R.C. Ewing, J.M. Farmer, L.A. Boatner, Acta Mater. 51 (2003) 1493.
[17] K.E. Sickafus, L. Minervini, R.W. Grimes, J.A. Valdez, M. Ishimaru, F. Li, K.J. McClellan, T. Hartmann, Science 289 (2000) 748.
[18] B.D. Begg, N.J. Hess, D.E. McCready, S. Thevuthasan, W.J. Weber, J. Nucl. Mater. 289 (2001) 188.
[19] J. Lian, X.T. Zu, K.V.G. Kutty, J. Chen, L.M. Wang, R.C. Ewing, Phys. Rev. B 66 (2002) 054108.
[20] M. Lang, F.X. Zhang, J.M. Zhang, J.W. Wang, B. Schuster, C. Trautmann, R. Neumann, U. Becker, R.C. Ewing, Nature Mater. 8 (2009) 793.
[21] A.J. Feighery, J.T.S. Irvine, C. Zheng, J. Solid State Chem. 160 (2001) 302.
[22] F.X. Zhang, M. Lang, U. Becker, R.C. Ewing, J. Lian, Appl. Phys. Lett. 92 (2008) 011909.
[23] F.X. Zhang, J. Lian, U. Becker, R.C. Ewing, J.Z. Hu, S. Saxena, Phys. Rev. B 76 (2007) 214104.
[24] F.X. Zhang, J. Lian, U. Becker, L.M. Wang, J. Hu, S. Saxena, R.C. Ewing, Chem. Phys. Lett. 441 (2007) 216.
[25] F.X. Zhang, J.W. Wang, J. Lian, M.K. Lang, U. Becker, R.C. Ewing, Phys. Rev. Lett. 100 (2008) 045503.
[26] F.X. Zhang, M. Lang, Z.X. Liu, R.C. Ewing, Phys. Rev. Lett. 105 (2010) 015503.
[27] R.S. Kumar, A.L. Cornelius, M.F. Nicol, K.C. Kam, A.K. Cheetham, J.S. Gardner, Appl. Phys. Lett. 88 (2006) 031903.
[28] R.C. Ewing, W. Weber, J. Lian, J. Appl. Phys. 95 (2004) 5949.
[29] M. Lang, F.X. Zhang, J.M. Zhang, J.W. Wang, J. Lian, W.J. Weber, B. Schuster, C. Trautmann, R. Neumann, R.C. Ewing, Nucl. Instrum. Methods B 268 (2010) 2951.
[30] F.X. Zhang, M. Lang, R.C. Ewing, J. Mater. Chem. in preparation.
[31] H.K. Mao, J. Xu, P.M. Bell, J. Geophys. Res. 91 (1986) 4673.
[32] A. Hammersley, Computer Program Fit 2d, ESRF, Grenoble, 1998.
[33] T. Roisnel, J. Rodriguez-Carvajal, Mater. Sci. Forum, in: Proceedings of the Seventh European Powder Diffraction Conference, EPDIC7, 118, 2000.
[34] J.W. Wang, F.X. Zhang, J. Lian, R.C. Ewing, U. Becker, Acta Mater. 59 (2011) 1607.
[35] F.X. Zhang, B. Manoun, S.K. Saxena, C.S. Zha, Appl. Phys. Lett. 86 (2005) 181906.
[36] S. Saha, D.V.S. Muthu, C. Pascanut, N. Dragoe, R. Suryanarayanan, G. Dhalenne, A. Revcolevschi, S. Karmakar, S.M. Sharma, A.K. Sood, Phys. Rev. B. 74 (2006) 064109.
[37] P. Richet, P. Gillet, Eur. J. Mineral 9 (1997) 907.